Time Variability of FUV Emission from Cool Stars on Multi-year Timescales

by

Leo Cole Kamgar

defended on April 4$^{\text{th}}$, 2023

A thesis submitted to
the Faculty of the University
of Colorado in partial fulfillment of
the requirements for the degree of
Bachelor of Arts
College of Arts and Sciences
2023

Committee Members:
Kevin France, Thesis Advisor, Department of Astrophysical & Planetary Sciences
Jun Ye, Honors Council Representative, Department of Physics
Dmitri Uzdensky, Department of Physics
David Malaspina, Department of Astrophysical & Planetary Sciences

Kamgar, Leo Cole (B.A.)

Time Variability of FUV Emission from Cool Stars on Multi-year Timescales

Thesis directed by Prof. Kevin France, Thesis Advisor, Department of Astrophysical & Planetary Sciences

The physical and chemical properties of planetary atmospheres are affected by temporal evolution of ultraviolet (UV) radiation inputs from their host stars at all time scales. This includes the short-lived flares ranging from minutes to hours, to medium-scaled stellar rotation and cycles ranging from days to years, and long-term stellar evolutionary changes on timescales of millions to billions of years. These varying energy inputs have great influence on the photochemical equilibrium of exoplanetary atmospheric conditions and their susceptibility to atmospheric escape. While studies of X-ray/UV flare properties and long-term stellar evolution of exoplanet host stars have provided new constraints regarding stellar inputs to exoplanetary systems, the UV temporal variability of cool stars on the timescale of stellar cycles remains largely unexplored. To address this concern, we analyze far-ultraviolet (FUV) emission lines of ions that trace the chromosphere and transition region of nearby stars (C II, Si III, Si IV, and N V; formation temperatures $\sim 20-150$kK) using data from the *HST* and *IUE* archives spanning temporal baselines of months to years. We select 33 unique stars of spectral types F – M with observing campaigns spanning over a year, and create ionic light curves to evaluate the characteristic variability of cool stars on such timescales. Screening for large flare events, we observe that the relative variability of FUV light curves, with such timescales, decreases with increasing stellar effective temperature, from $30-70\%$ variability for M-type stars to $< 30\%$ variability for F and G-type stars. We also observe a weak trend in the temporal variability with the Ca II R'_{HK} stellar activity indicator, suggesting that stars with lower Ca II activity exhibit a smaller range of FUV flux variability. Screening for data sets with optimal temporal spread, and a sufficient number of individual observations, we select 5 data sets for further periodicity analysis (*HST* α Centauri A, *HST* α Centauri B, *IUE* α Centauri B, *IUE* ϵ Eri, *IUE* ξ Boo). Various periodic structures within the FUV flux were detected, with most significant being a 79 day frequency present within *IUE* ξ Boo, with a significance of 6-σ. Additional periodic structure of high significance was detected within α Centauri B, for both *HST* and *IUE* measurements being a 210 day frequency with significance of 3-σ and 3.7-σ, respectively. Periodicities detected require further examination to identify potential false-periodic sources, such as measurement frequency. Our results suggest that extreme ultraviolet (EUV) flux from cool stars varies by less than a factor of two on decade timescales, as EUV flux is known to correlate tightly with N V and Si IV.

Contents

Tables

Table

Figures

Figure

March 2023

Chapter 1

Introduction

The study of exoplanets, or planets outside of our own solar system, has undergone many technological advancements that have revolutionized the field of astronomy within the past three decades. 16th century astronomers hypothesized their existence, however, it wasn't until the 1990's that the discovery of the first exoplanet was confirmed (Mayor & Queloz, 1995).

Initial exoplanet detections were mostly large gas giants. They were similar in size to Jupiter or Saturn, and very close to their host stars, as this allowed detection using the radial velocity method. This method involves the observation of wobbling motion of a star as a result of the mutual gravitational influence of its orbiting planet. However, as technology advanced, astronomers became able to detect even smaller exoplanets using the transit method. This involves the observation of the periodic dips of a host star's brightness as a result of an orbiting planet partially eclipsing it (Charbonneau et al., 1999).

Advancements lead to the development of the Kepler Space Telescope (KST), which launched in 2009, playing an instrumental role in exoplanet research. With its space platform, the KST is able to perform long monitoring observations of an individual field of stars. Additionally, the lack of atmospheric disturbances has allowed the KST to detect thousands of exoplanet candidates using the previously defined methods. Some of these systems are Earth-sized exoplanets within habitable zones of many solar systems (Dressing & Charbonneau, 2015).

Additional recent developments include the use of space telescopes like Transiting Exoplanet Survey Satellite (TESS) and the James Webb Space Telescope (JWST). These new instruments have enabled scientists to find exoplanets within our solar neighborhood, and study them in greater detail. This detail has afforded increasingly precise measurements on their atmospheres (Ahrer et al., 2023) and potential habitability. This progress made in exoplanet research has furthered our understanding of the universe, as well as our place within it.

As a result of the ever-expanding number and diversity of exoplanet detections, it has become abundantly clear that a shift from an era of exoplanet discovery to an era of characterization is necessary. The study of exoplanet atmospheric evolution is needed to understand how their properties evolve over the lifetimes of these planets. Therefore our goal has pivoted toward analyzing and understanding exoplanetary atmospheric composition and evolution. This can then be used for identifying those that may potentially support habitable atmospheric conditions.

Of the factors that drive atmospheric composition and evolution, the most critical is the interaction between exoplanetary atmospheres and their host star's light. Starlight is the primary energy source that drives photochemistry, heating, and cooling within atmospheres (Tsai et al., 2022). The radiative transfer properties, of these exoplanetary atmospheres, are determined by the absorption and scattering of light by atmospheric gasses. This process then influences the temperature and pressure profiles of these planets. Furthermore, the interactions between starlight and exoplanetary atmospheres drive atmospheric escape processes, which are a dominant factor in the evolution of these planets (Lammer et al., 2003).

Ultraviolet (UV) radiation plays a central role in the photochemical reactions on both gaseous and rocky exoplanets. UV photons ionize and dissociate molecular species in the upper atmosphere, which in turn leads to the formation of radicals and ions. These molecular species can then participate in numerous chemical reactions (Tsai et al., 2022).

For rocky planets, UV radiation is a driving factor in the formation of ozone, a molecule necessary for blocking harmful UV radiation from reaching the surface of a planet. Ozone, is formed by a series of photochemical reactions that begin with the dissociation of molecular oxygen by UV. These resulting oxygen atoms will react with molecular oxygen to form ozone (Harman et al., 2015).

In addition to UV's contribution on rocky planets, it is a significant source of formation of haze particles in the upper atmosphere of Jovian and Neptunian planets. These haze particles are formed by photochemical interactional processes involving simple organic molecules, such as methane and nitrogen, by high-energy photons. The precise mechanisms involved with haze formation are not completely understood. However, it is thought to involve complex photochemical pathways that produce a range of organic molecules, some of which can condense into small particles that scatter light (see, e.g., Teal et al. 2022 and references therein).

As a result of the significant coupling between UV radiation and exoplanetary atmospheric conditions, understanding the host stars UV spectrum, and how it changes with time, becomes critical for interpreting observational data and identifying potential biosignatures in these environments.

Photochemistry, as driven by UV radiation, can also lead to the heating of an exoplanet's atmosphere. This increase in temperature directly increases the atmospheric escape rate. When an atmosphere becomes heated, gaseous atoms within the atmosphere begin to move faster. These faster speeds allow for more energetic atoms to escape the atmosphere completely, leading to greater atmospheric escape rates. This process can ultimately lead to a planet losing its atmosphere entirely, likely rendering it uninhabitable (Tian et al., 2008; Jakosky et al., 2018).

The intensity of UV radiation, as received by an exoplanet, depends on the host star's spectral type and age. For example, M-type dwarf stars are known to emit a significant amount of UV radiation in the form of flares, which can lead to potentially extreme atmospheric heating and escape (France et al., 2016). On the other hand, G-type stars, similar to our Sun, emit less UV radiation as a fraction of their total luminosity. As a result, they are far less likely to drive significant atmospheric heating and escape.

The absorption of UV radiation is directly linked to the generation of ions in a star's upper atmosphere. The Si^{2+}, N^{4+}, C^{+}, and Si^{3+} ions are formed within the chromosphere and transition region of a star, where solar magnetic processes heat the gas. This heating, in turn, is followed by higher electron collision rates, which leads to a highly ionized plasma. The result is the creation of these ions, with electrons that are constantly transitioning from their ground states to excited states, via electron collisions. Subsequently, these excited electrons drop back down to their ground state, releasing a photon with a wavelength corresponding to the energy drop between electron states. This photon emission creates unique emission lines, Si III, N V, C II, and Si IV (corresponding to each ion, respectively), that can be observed and studied by astronomers.

The intensity of the transitions for each of these ions is related to the level of magnetic heating, with higher intensities indicating greater heating. As a result, the analysis of the emission lines of Si III, N V, C II, and Si IV allows astronomers to better understand the nature of the UV radiation present in a star's atmosphere.

In summary, the complex interaction between a host star's light and its exoplanets' atmospheres are a significant contributor to the atmospheric composition and evolution of these exoplanets. Therefore, the aim of this study is to perform extensive UV monitoring, via the Si III, N V, C II, and Si IV emission line observations, of FGKM stars, in efforts of identifying potentially habitable atmospheres beyond our own solar system.

FGKM stars, which include F, G, K, and M spectral types, are a group of the most prevalent stars in the universe ($\sim 90\%$ of all stars), commonly known as 'cool stars'. They are of particular interest to astronomers for their similarities with our own Sun in terms of size, mass, and temperature. The mass range of FGKM stars is approximately $\sim 2 - 0.1 M_{\rm Sun}$, with F stars being the most massive of this group ($\sim 1 - 2 M_{\rm Sun}$) and M stars being the least massive ($\sim 0.1 - 0.6 M_{\text{Sun}}$). Because FGKM stars are relatively smaller and cooler than larger, hotter stars, they are favorable for the transit method of exoplanet detection (where the signal is proportional to the ratio of the planetary to stellar surface area).

Another advantage of FGKM stars are their relative stability and long lifetimes. These stars have lifetimes that are orders of magnitude longer than larger, hotter stars, providing ample time for exoplanets to develop, form, and evolve in their stable environments.

The increased emphasis in exoplanet atmospheric characterization has highlighted a gap in our knowledge of cool stars and their temporal variability. Although numerous studies on flare events of individual stars have been published, there are no comprehensive studies on the longer-term temporal variability of cool stars. As a result, little is known about the UV variability of planet-hosting stars on timescales of stellar rotation or planetary orbits, e.g., timescales of months to years.

In efforts to address this gap, a study on the temporal variance of the UV profile of host stars has become necessary for the further research and development of models concerning the habitability of exoplanetary atmospheres. This particular study aims to provide information on the longer-term temporal variability of cool stars, which can aid in the prioritization of stars for the observation of habitable exoplanets. With the use of direct imaging techniques planned for the Habitable Worlds Observatory (HWO), NASA requires information that better determines which stars are the most promising targets to maximize the chances of detecting and characterizing habitable exoplanets. This study will provide inputs to NASA's target selection and habitable planet detection strategies for future missions.

This honors thesis presents the first comprehensive investigation of the temporal UV variability of cool stars on timescales of months to years with an archival study of UV spectroscopic observations made over the long missions of the Hubble Space Telescope (HST) and the International Ultraviolet Explorer (IUE). This study analyzes the emission lines Si III, N V, C II, and Si IV, spectral features formed in the hot upper atmospheres of cool stars. By analyzing how these spectral emission features evolve in time, this study characterizes the

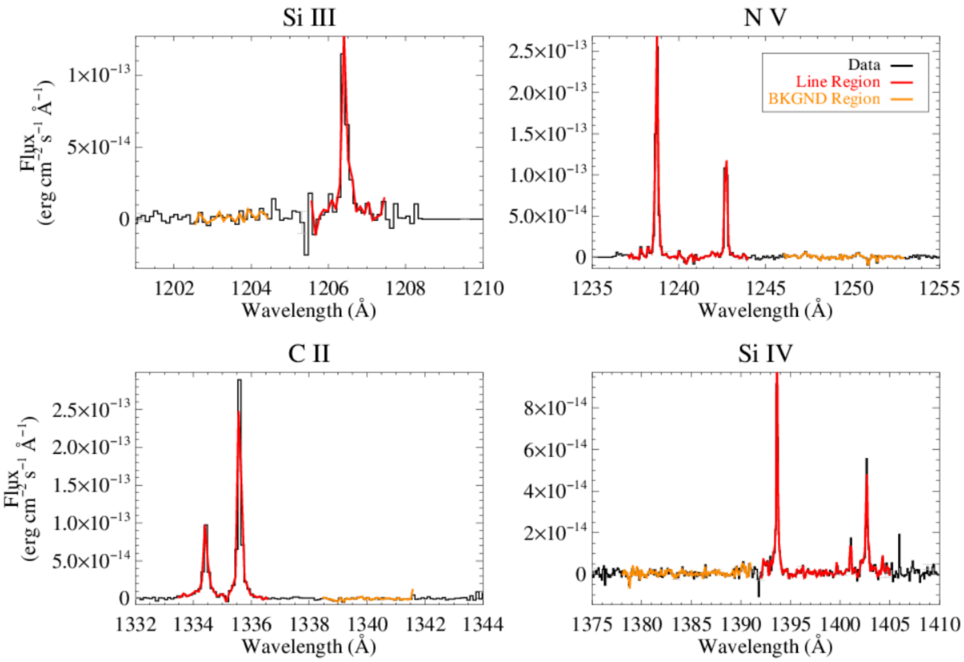

Figure 1.1: Example *HST*-STIS spectra of Proxima Cen (M5.5 V) showing the emission line measurement regions around Si III, N V, C II, and Si IV. The black histogram is the STIS E140M data. The final emission fluxes are the numerically-integrated on-line region (shown in red) with the nearby instrumental/continuum background subtracted (the background region is shown in orange).

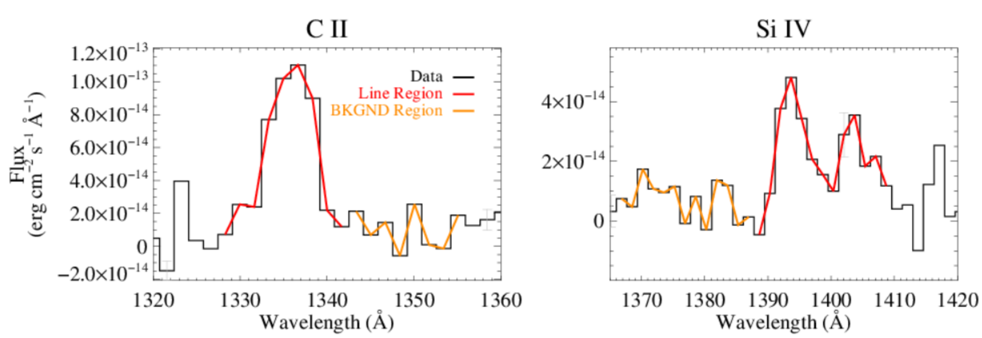

Figure 1.2: Example *IUE* spectrum of ϵ Eri (K2 V) showing the emission line measurement regions around C II and Si IV. The black histogram is the *IUE* data. The final emission fluxes are the numerically-integrated on-line region (shown in red) with the nearby instrumental/continuum background subtracted (the background region is shown in orange). We do not measure Si III and N V in the *IUE* data owing to a large contribution from scattered geocoronal and stellar Lyman-α.

UV variability of these stars and explores the correlation with the degree of UV variability with the mass and magnetic activity levels of the stellar sample.

Chapter 2

UV Spectroscopic Observations and Data Reduction

Measurements were performed via a comprehensive search of the Mikulski Archive for Space Telescopes (MAST) to identify multi-epoch far-ultraviolet spectroscopic observations of cool stars of spectral types F – M. There was strict criteria imposed on the search, being that the mission must contain long-term data observation of a star with simultaneous coverage over a range of formation temperatures (ranging from $\sim 20 - 150$kK, corresponding to observation of C II, Si III, Si IV, N V emission lines). The missions that met the requirements were the *Hubble Space Telescope* (*HST*)-Space Telescope Imaging Spectrograph (STIS) and -Cosmic Origins Spectrograph (COS) instruments, as well as the *International Ultraviolet Explorer* (*IUE*). Unfortunately, many other FUV spectroscopic instruments, such as the Hopkins Ultraviolet Telescope, and earlier generation UV spectrographs on *HST* lacked either the necessary long-term multi-epoch data sets, or spectral coverage, which hindered a uniform data set for emission line monitoring. Following France et al. (2018), our central focus remains ion emission bands for Si III, N V, C II, and Si IV, which are visible at wavelengths, 1206 Å, 1238 & 1243 Å, 1335 Å, and 1394 & 1403 Å, and corresponding $\log_{10}(T_{form})$'s of 4.7, 5.2, 4.5, and 4.8, respectively (T_{form} is the formation temperature of the ion that generates the emission line). Reasoning for this select focus is because of the wide-spread of formation temperature, spanning nearly an order of magnitude (assuming collisional electron excitation; Dere et al. (2009)), and they are the brightest metal lines available in the FUV spectrum of FGKM stars covered by *IUE*, the *HST*-STIS E140M mode, and the most widely used HST-COS mode for cool star observations, G130M.

Measurements were further constrained, by utilizing the different object classifications of cool stars available within MAST. As a result, only objects with FUV spectroscopic data sets covering a temporal baseline of at least one year (the average returned data set spans: 3793 days), with a minimum of five individual visits to the target in total. Following this, an initial visual inspection was then conducted on a subset of each target's spectroscopic data to ensure the data quality would be high enough for reliable emission line measurements. With these filters and inspections in place, numerous cool star monitoring programs from IUE (Ayres, 1991; Teal et al., 2022), and exoplanet host star monitoring or transit programs with HST (MacGregor et al., 2021; Loyd et al., 2023), were identified. The final list of potential targets then underwent an additional screening for interacting binary stars (e.g. RS CVn systems) before downloading the full multi-epoch data sets from MAST. Ultimately, this process had yielded us a final sample of 9 stars from HST and 29 stars from IUE, with some stars overlapping both data sets. The stellar sample is presented in Table 2.2, leaving us with all the data sets that met the criteria, with temporal baselines ranging from approximately 1 to 20 years and 5 – 200 visits per star.

Given the FUV spectroscopic data, further analysis was on a per-exposure basis, in order to extract the relevant emission line fluxes of the four ionic trandsitions tracing the chromosphere and transition region activity studied here. For the instruments employing first-order spectrometers (HST-COS and IUE), the flux and wavelength-calibrated data were able to be directly analyzed. However, for HST-STIS echelle data, the multiple orders of data were combined into a single one-dimensional flux and wavelength-calibrated spectrum before analysis took part. In order to measure the emission line fluxes, numerical integration was performed on the wavelength region containing the line of interest (visible in the red regions in Figures 1.1 and 1.2) and stored as F_{ion}. The uncertainty within the measurement is stored as Err_{ion}, before subtracting a nearby continuum/background region of the same spectral width (visible in the orange regions in Figures 1.1 and 1.2) and stored as B_{ion}. In efforts to minimize randomized noise and poor data measurements, further data refinement occurred. Setting a detection threshold for including an individual measurement of k, a filter for data points is as provided: $F_{ion,k} - Err_{ion,k} > 1.3 - 2.0\times\ B_{ion,k}$, depending on the spectral type of the target star. Subsequently, arrays of line fluxes measured were analyzed for data quality issues, such as guide star acquisition failures that result in the stellar flux being comparable to the background level, as the telescope is most likely misaligned to the target (results in excluding points with $F_{ion,k} < 0.2 \langle\ F_{ion}\ \rangle$). Finally, these time-resolved emission line fluxes constitute the spectroscopic lightcurves (Table 2.3) that were then analyzed for further understanding of the long-term variability of the FUV output of nearby cool stars, as described in Section 3.

Table 2.1: Star Parameters

Star	$B-V$	T_{eff}	P_{rot}	$\log(R'_{HK})$	Sources
α CMi	0.42	6474	23	-4.11	1,2
β Cas	0.34	6959	1.1	-4.27	1,2
BH CVn	0.4	6653	–	-3.84	1,2
ϵ Aur	0.54	7395	–	–	1
ϵ CrA	0.36	6647	–	–	1
h UMa	0.33	7096	0.85	-3.99	1,2
α Centauri A	0.71	5788	–	-5.15	1,2
HD 209458	0.58	6118	14.4	-4.88	1,2
E Vir	–	5999	3.3	-4.30	1,2
AR Lac	0.72	5342	–	–	1
EK Dra	0.639	5845	2.606	-4.02	1,2
ξ Boo	0.777	5511	6.43	-4.30	1,2
α Centauri B	0.88	–	36.2	-4.97	1,2
HD 189733	0.93	5044	13.4	-4.51	1,2
AB Dor	0.857	5273	0.5	-3.88	1,2
CC Eri	1.336	3831	–	-3.78	1,2
ϵ Eri	0.88	–	11.7	-4.51	1,2
36 Oph B	0.85	5199	–	-4.74	1,2
70 Oph	0.86	5419	19.7	-4.12	1,2
HD 17925	0.86	5115	6.6	-4.30	1,2
LQ Hya	0.87	–	1.6	-3.97	1,2
UX Ari	0.91	5041	6.4	–	1
HD 283750	–	4405	1.8	–	1
AU Mic	1.423	3518	4.85	-3.88	1,2
Ross 905	1.447	3353	48	-5.09	1,2
Proxima Centauri	1.82	2810	83	-4.30	1,2
BD+20 2465	1.3	2991	–	-4.00	1,2
BD+19 5116	1.584	3630	1.06	–	1
EV Lac	1.59	3167	–	-3.75	1,2
HD 152751	1.57	3441	–	-4.20	1,2
V1005 Ori	1.373	3661	4.4	–	1
YY Gem	1.29	3885	–	–	1
YZ CMi	1.606	3088	2.77	-3.47	1,2

Star parameter data for each unique star within study. T_{eff} (Effective Temperature) is measured in ($^{\circ}K$) and P_{rot} (Rotational Period) in ($days$). Sources: 1. SIMBAD Astronomical Database 2. Boro Saikia, S. et al. (2018)

Table 2.2: Star Data Collection

Star	Instr.	N	Start	End	Δ
β Cas	IUE	50	43743.2	48822.7	5079.5
BH CVn	IUE	6	44024.7	49166.8	5142.1
ϵ Aur	IUE	84	43731.7	46156.0	2424.3
h UMa	IUE	3	47963.9	49389.9	1426.0
α CMi	HST	5	55656.109	55864.76	208.651
ϵ CrA	IUE	16	44157.4	45056.7	899.3
AR Lac	IUE	223	44011.4	49631.5	5620.1
EK Dra	IUE	18	45152.2	49893.3	4741.1
α Centauri A	IUE	188	43737.2	49935.6	6198.4
E Vir	IUE	20	45011.6	49890.8	4879.2
HD 209458	HST	21	55093.424	57520.977	2427.553
ξ Boo	IUE	62	43644.4	49132.9	5488.5
α Centauri A	HST	15	55220.219	58011.661	2791.442
ϵ Eri	IUE	73	43743.6	48480.7	4737.1
α Centauri B	IUE	77	43737.5	49931.6	6194.1
LQ Hya	IUE	26	45283.2	49345.1	4061.9
36 Oph B	IUE	3	44506.4	48136.5	3630.1
CC Eri	IUE	19	47795.8	48251.7	455.9
UX Ari	IUE	66	43735.6	50104.9	6369.3
α Centauri B	HST	9	55378.037	56862.925	1484.888
HD 189733	HST	8	55090.772	59093.266	4002.494
HD 17925	IUE	13	44892.4	49694.9	4802.5
70 Oph	IUE	15	44436.8	48148.0	3711.2
AB Dor	IUE	30	45082.0	48255.8	3173.8
HD 283750	IUE	10	44611.0	48660.9	4049.9
HD 152751	IUE	13	44466.0	48314.6	3848.6
HD197481	HST	4	51062.512	51062.704	0.192
Ross 905	HST	15	56101.308	58177.314	2076.006
Proxima Centauri	HST	54	51672.04	58665.058	6993.018
BD+20 2465	HST	6	51613.145	52427.233	814.088
EV Lac	IUE	20	44849.6	49241.7	4392.1
HD197481	IUE	82	44122.8	48874.6	4751.8
BD+19 5116	IUE	22	43858.0	48861.9	5003.9
Proxima Centauri	IUE	14	43921.7	49927.7	6006.0
YZ CMi	IUE	40	43922.1	49708.2	5786.1
V1005 Ori	IUE	10	44525.7	48677.9	4152.2
YY Gem	IUE	63	45303.4	48349.3	3045.9
BD+20 2465	IUE	57	45138.7	48385.2	3246.5

Star data collection statistics. Instr. indicates the instrument used for measurement. N is number of total measurements. Start and End are the Modified Julian Date days of the first and last measurement, respectively. Δ in (*days*), is the length of observation.

Table 2.3: Collective Flux Measurements for Select Stars

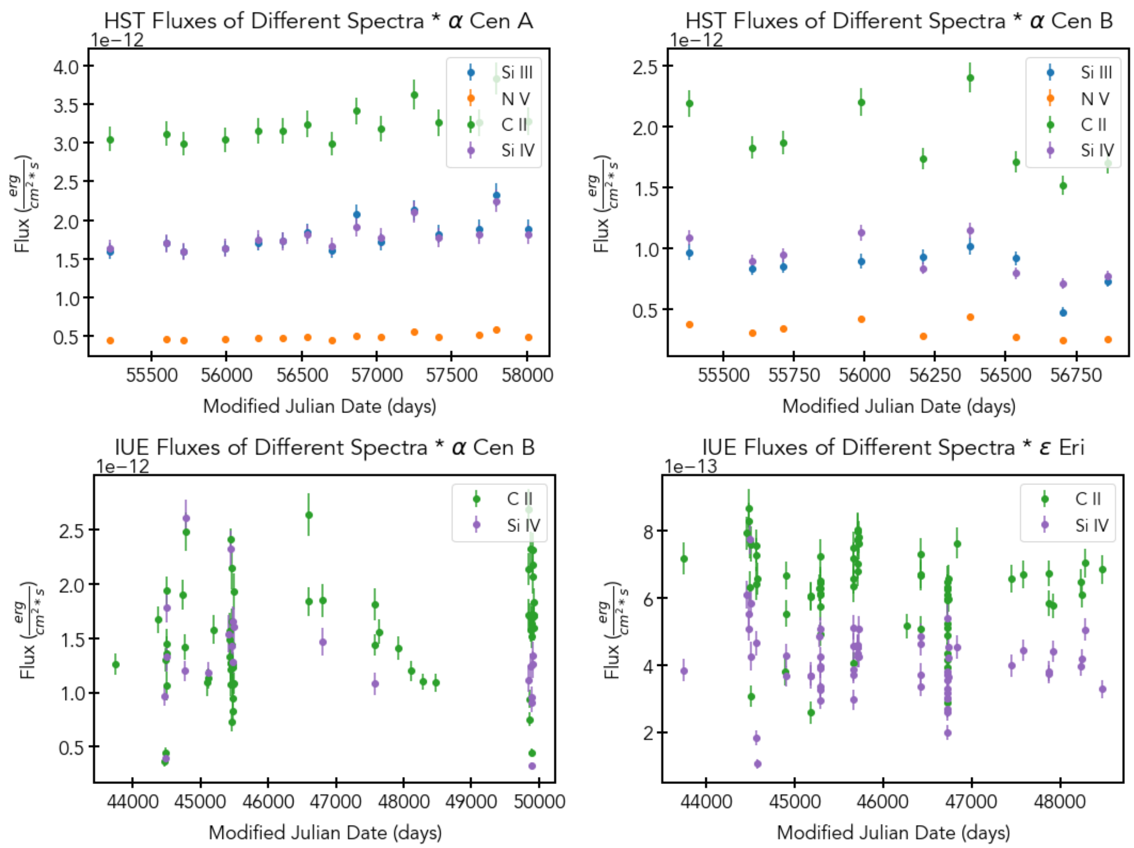

HST & IUE measurements for various stars, including Si III, N V, C II, and Si IV ion emission bands.

Chapter 3

FUV Lightcurves and Analysis

3.1 Relative Variability/Maximum Linear Regression Analysis

The calculations for the relative variability and maximum variability were computed by performing standard statistical techniques on the various samples of data. In practice, these calculations for the HST and IUE data were processed via the numpy[1] software package. To start, for each star we are provided with a 2-dimensional data set for each ion:

$$\{[t_1, f_1 \pm E[f_1]], \cdots, [t_n, f_n \pm E[f_n]]\}_{ion}$$

where f_i denotes some measured flux output (of which there are n measurements), with associated measurement error, $E[f_i]$, corresponding to the time of measurement, t_i. We start with the simplest statistical calculations for the sample mean, μ, standard deviation, σ, and maximum, α, for each ion:

$$\mu = \frac{\sum_{i=1}^{n} f_i}{n} \tag{3.1}$$

$$\sigma = \sqrt{\frac{\sum_{i=1}^{n} (f_i - \mu)^2}{n}} \tag{3.2}$$

$$\alpha = \mathrm{Max}\{f_1, \cdots, f_n\} \tag{3.3}$$

[1] Scientific computing python package `https://numpy.org/`.

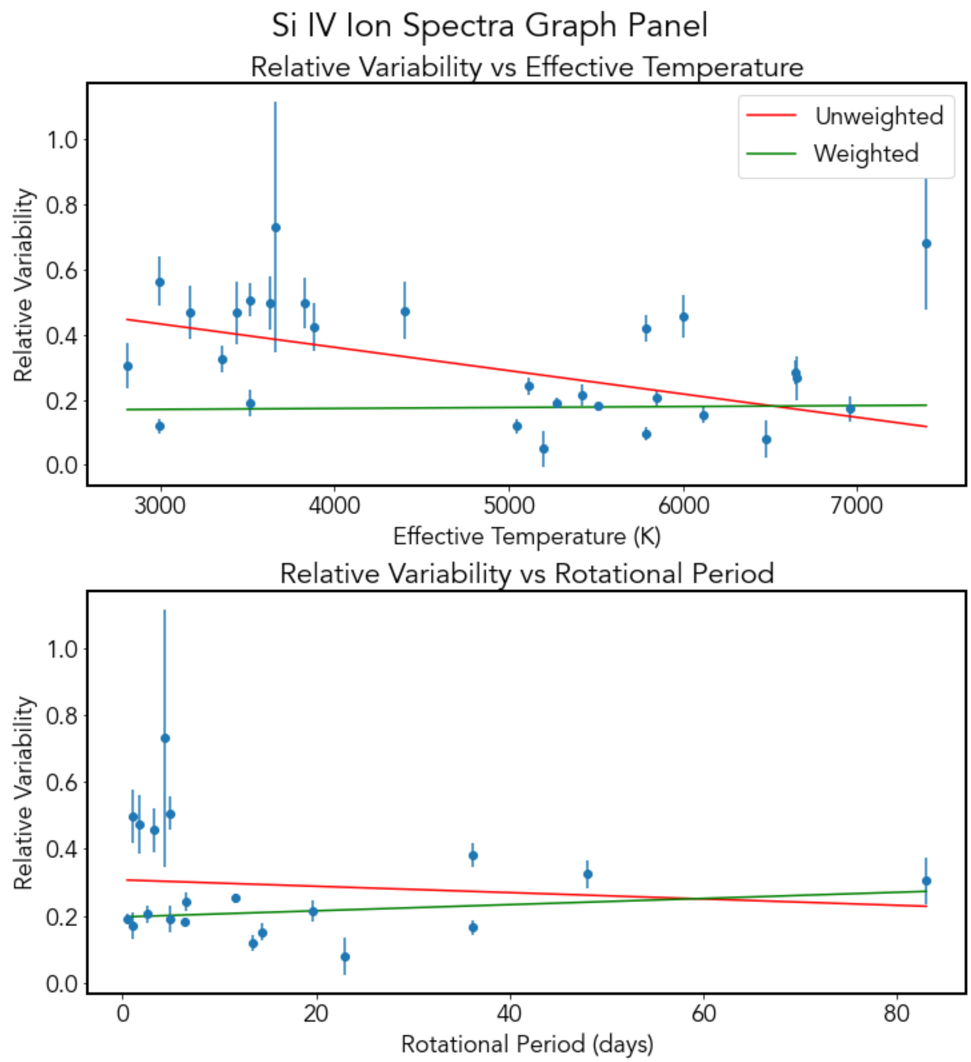

Figure 3.1: Si IV ion emission correlations with parameters for weighted vs. unweighted distinguished by subscript w & u, respectively. Relative Variability vs Effective Temperature (top), with linear parameters: $\beta_{0_w} = 0.1616 \pm 0.0779$, $\beta_{1_w} = (2.9095 \pm 1.4424)10^{-6}$, $\beta_{0_u} = 0.6476 \pm 0.1148$, $\beta_{1_u} = (-7.167 \pm 2.3692)10^{-5}$. Relative Variability vs Rotational Period (bottom), with linear parameters: $\beta_{0_w} = 0.1968 \pm 0.0143$, $\beta_{1_w} = 0.0009 \pm 0.0012$, $\beta_{0_u} = 0.3076 \pm 0.0485$, $\beta_{1_u} = 0.000 + / - 0.0018$.

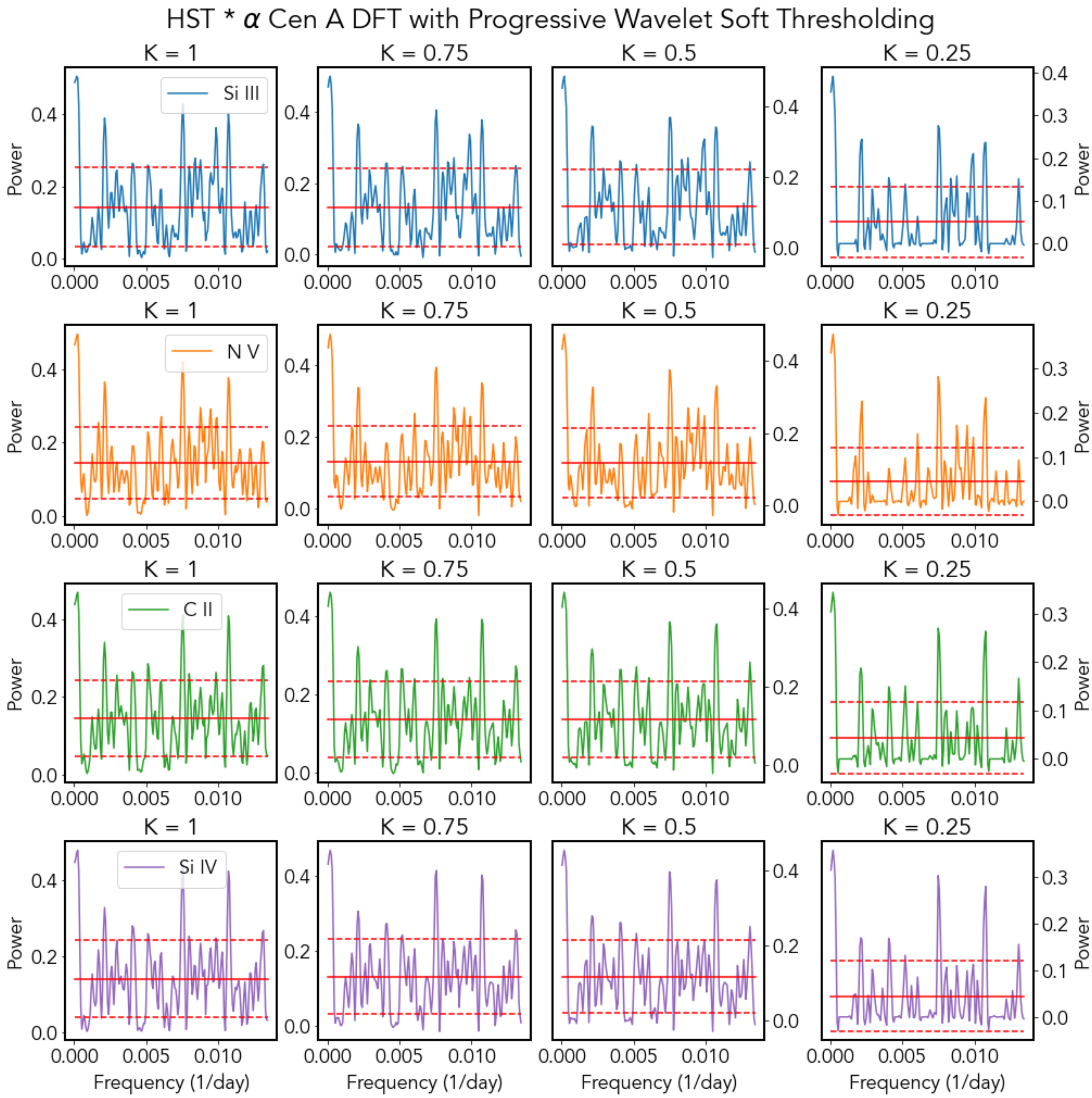

Figure 3.2: Discrete Fourier transform of HST α Centauri A for each ion is displayed in the left-most column. Each subsequent column represents progressively greater wavelet soft thresholding. K (Keep coefficient) is % of wavelet coefficients above threshold. The columns are, from left to right, 100%, 75%, 50%, 25%, respectively.

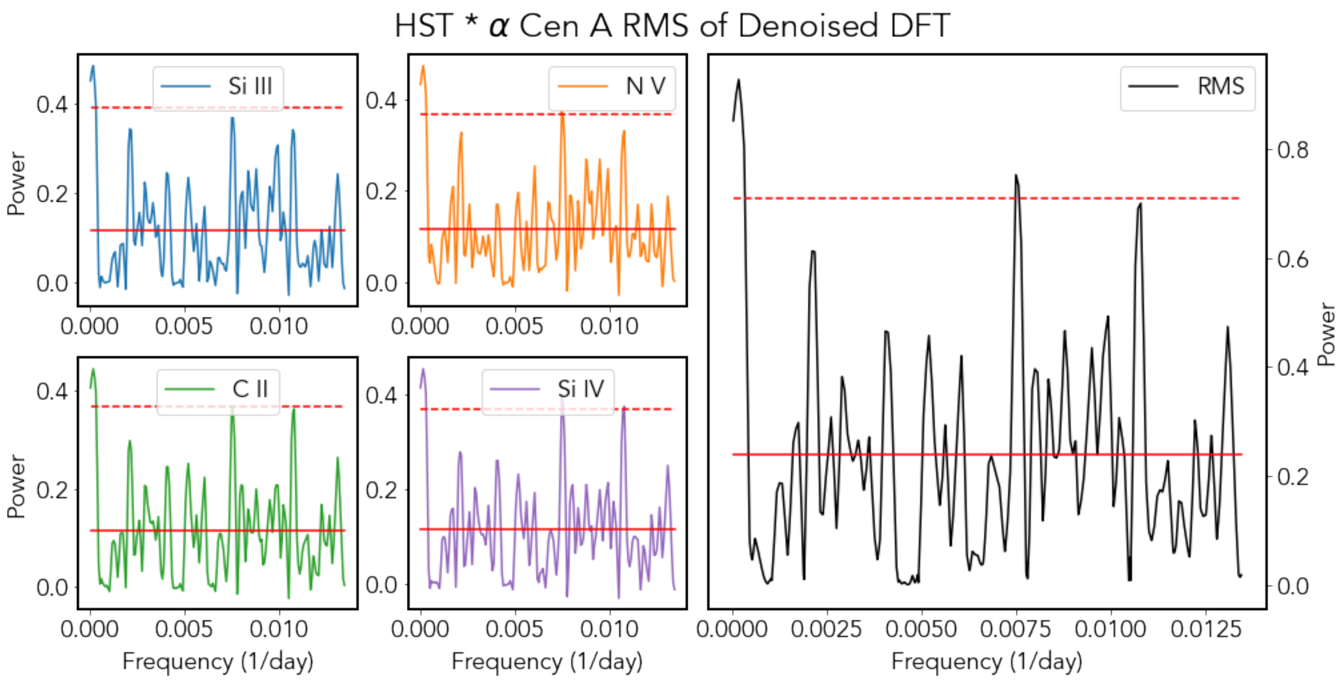

Figure 3.3: Discrete Fourier transform of HST α Centauri A, with a wavelet soft threshold of $K = 0.5$ (left 4). Root-mean-square combination of all ions (right).

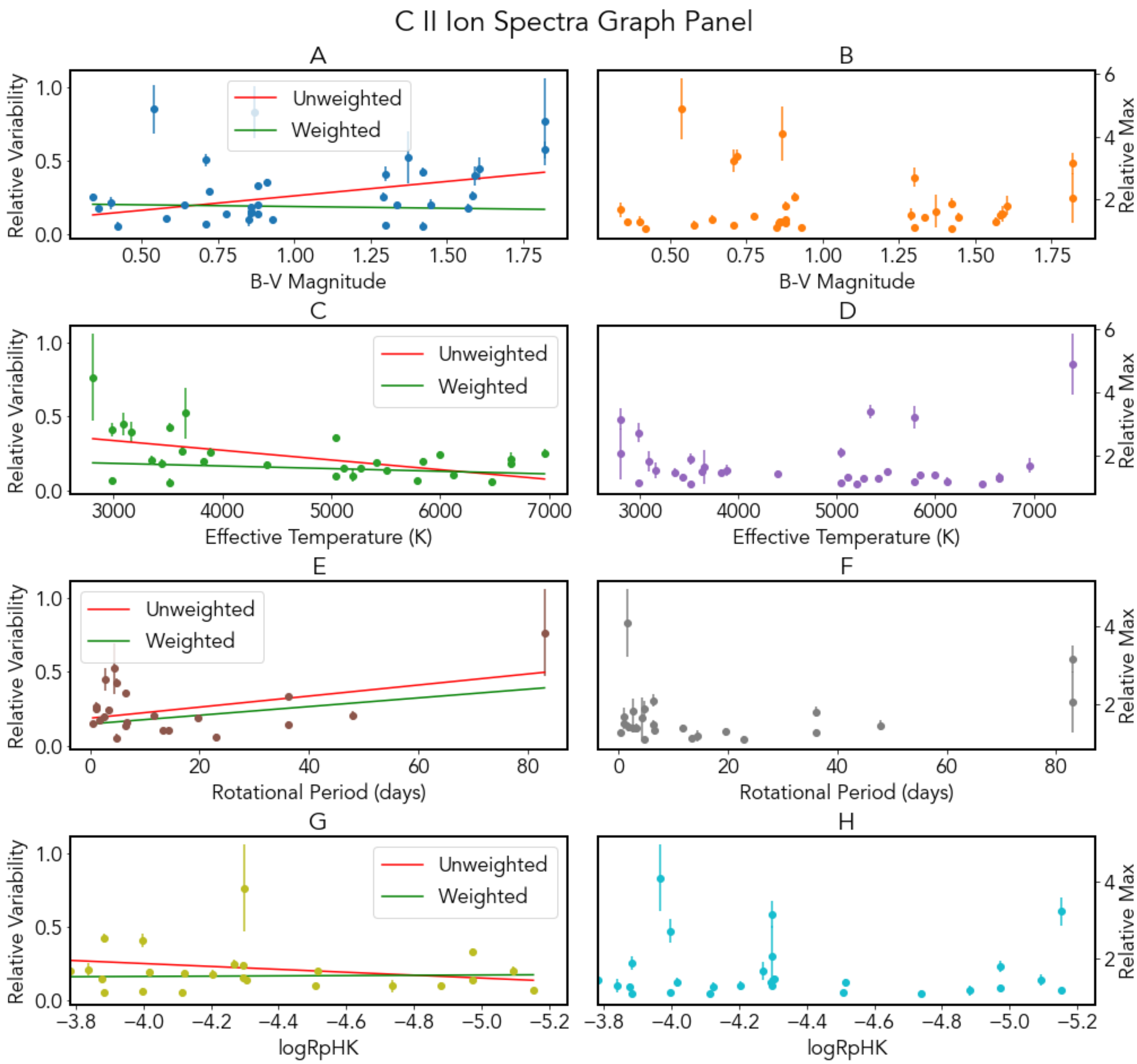

Figure 3.4: Full C II ion emission correlations with parameters for weighted vs. unweighted distinguished by subscript w & u, respectively. (A) $\beta_{0_w} = 0.2129 \pm 0.0756$, $\beta_{1_w} = 0.023 \pm 0.0904$, $\beta_{0_u} = 0.0662 \pm 0.0888$, $\beta_{1_u} = 0.1957 \pm 0.0777$, (C) $\beta_{0_w} = 0.2363 \pm 0.0754$, $\beta_{1_w} = (-1.788 \pm 1.4007)10^{-5}$, $\beta_{0_u} = 0.5351 \pm 0.1039$, $\beta_{1_u} = (-6.589 \pm 2.1859)10^{-5}$, (E) $\beta_{0_w} = 0.1462 \pm 0.0157$, $\beta_{1_w} = 0.0029 \pm 0.0012$, $\beta_{0_u} = 0.1855 \pm 0.0439$, $\beta_{1_u} = 0.0037 \pm 0.0017$, (G) $\beta_{0_w} = 0.1265 \pm 0.1525$, $\beta_{1_w} = 0.009 \pm 0.0345$, $\beta_{0_u} = 0.6470 \pm 0.3103$, $\beta_{1_u} = 0.0986 \pm 0.0718$

Given these simple statistical variables, we define further statistical variables, relative variability, σ_{rel}, and relative maximum, α_{rel}, as:

$$\sigma_{rel} \equiv \frac{\sigma}{\mu} \tag{3.4}$$

$$\alpha_{rel} \equiv \frac{\alpha}{\mu} \tag{3.5}$$

In order to get the associated errors with each of these calculated variables, we use the division and multivariate error propagation formulas. Given some division variable of the following form:

$$U(X,Y) = \frac{X}{Y}$$

We have an associated error:

$$E[U] = U\sqrt{\left(\frac{E[X]}{X}\right)^2 + \left(\frac{E[Y]}{Y}\right)^2} \tag{3.6}$$

Given some multivariate variable:

$$U\left(X_1, \cdots, X_k\right)$$

We have an approximate associated error:

$$E[U] \approx \sqrt{\sum_{i=1}^{k} \left(\frac{\partial U}{\partial X_i}\right) E[X_i]} \tag{3.7}$$

Following from this, we can now calculate for the error within the relative variability and relative maximum. Plugging in the relative variability into Equation 3.6:

$$E[\sigma_{rel}] = \sigma_{rel}\sqrt{\left(\frac{E[\sigma]}{\sigma}\right)^2 + \left(\frac{E[\mu]}{\mu}\right)^2} \tag{3.8}$$

We now must calculate for $E[\sigma]$ & $E[\mu]$, however, the error in a mean is the standard error of the mean for a particular sample, given by:

$$E[\mu] = \frac{\sigma}{\sqrt{n}} \tag{3.9}$$

The error in the standard deviation can be derived by plugging in Equation 3.2 into Equation 3.7:

$$E[\sigma] \approx \sqrt{\sum_{i=1}^{n} \left(\frac{\partial \sigma}{\partial f_i}\right)^2 E[f_i]^2} \tag{3.10}$$

To calculate the partial derivative of the standard deviation with respect to each measurement, we plug in Equation 3.2 and get:

$$\begin{aligned}
\frac{\partial \sigma}{\partial f_i} &= \frac{\partial}{\partial f_i} \sqrt{\frac{1}{n} \sum_{i=1}^{n} (f_i - \mu)^2} \\
&= \frac{1}{2\sqrt{n}} \left(\sum_{i=1}^{n} (f_i - \mu)^2 \right)^{-1/2} \frac{\partial}{\partial f_i} \sum_{i=1}^{n} (f_i - \mu)^2 \\
&= \frac{1}{2n} \left(\frac{1}{n} \sum_{i=1}^{n} (f_i - \mu)^2 \right)^{-1/2} 2\left(f_i - \mu\right)
\end{aligned}$$

which simplifies to:

$$\frac{\partial \sigma}{\partial f_i} = \frac{f_i - \mu}{n\sigma} \tag{3.11}$$

Now that we have the partial derivative of the standard deviation, we can solve for the complete error of the standard deviation by plugging Equation 3.11 into Equation 3.10:

$$E[\sigma] \approx \frac{\sqrt{\sum_{i=1}^{n} \left(f_i - \mu\right)^2 E[f_i]^2}}{n\sigma} \tag{3.12}$$

Given all the pieces of the equation have been solved, we can return to the error in the relative standard deviation formula, by plugging Equations 3.12 and 3.9 into Equation 3.8:

$$E[\sigma_{rel}] \approx \sigma_{rel}\sqrt{\left(\frac{\sqrt{\sum_{i=1}^{n}(f_i-\mu)^2 E[f_i]^2}}{n\sigma^2}\right)^2 + \left(\frac{\sigma}{\sqrt{n}\mu}\right)^2}$$

which simplifies to our final equation for the error in relative variability:

$$E[\sigma_{rel}] \approx \sigma_{rel}\sqrt{\frac{\sum_{i=1}^{n}(f_i-\mu)^2 E[f_i]^2}{n^2\sigma^4} + \frac{\sigma_{rel}^2}{n}} \tag{3.13}$$

In order to obtain the error in relative maximum, we begin with the same process of plugging in Equation 3.5 into 3.6:

$$E[\alpha_{rel}] = \alpha_{rel}\sqrt{\left(\frac{E[\alpha]}{\alpha}\right)^2 + \left(\frac{E[\mu]}{\mu}\right)^2}$$

Utilizing $E[\alpha] = E[f_j]$ such that measurement j is the maximum, and Equation 3.9, we get:

$$E[\alpha_{rel}] = \alpha_{rel}\sqrt{\left(\frac{E[f_j]}{\alpha}\right)^2 + \frac{\sigma_{rel}^2}{n}} \tag{3.14}$$

Provided with the relative variability, relative maximum, their associated errors, and stellar parameters, the linear regression fits between the UV observables and the stellar characteristics were calculated. This is done by compiling complete data set for each ion:

$$\{[X_1, \sigma_{rel1} \pm E[\sigma_{rel1}]], \cdots, [X_n, \sigma_{reln} \pm E[\sigma_{reln}]]\}_{ion}$$

and

$$\{[X_1, \alpha_{rel1} \pm E[\alpha_{rel1}]], \cdots, [X_n, \alpha_{reln} \pm E[\alpha_{reln}]]\}_{ion}$$

where X_i is some star parameter for the i^{th} star in the complete sample. The linear regression minimizes the sum of the distance^2 to every point in the data set to a reference model. The weighted sum of squares (WSS) is defined to keep track of the sum of the distance^2:

$$WSS\left(\beta\right) = \sum_{i=1}^{n} w_i\left(y_i - \beta_0 - x_i\beta_1\right)^2 \tag{3.15}$$

where w_i = weight of each individual point, x_i and y_i represent data points, β_0 = intercept of a line, and β_1 = slope of a line. For each data set, a plot is made for both a weighted and unweighted linear fit. The weighted and unweighted fits use the corresponding weights:

$$w_i = \frac{1}{E[y_i]^2}$$

$$w_i = 1$$

respectively. The solution for the best-fit line comes down to optimizing for the minimum WSS with respect to the β parameters. This is done by constructing matrices:

$$\mathbf{y} = \begin{pmatrix} y_1 \\ \vdots \\ y_n \end{pmatrix}, \mathbf{X} = \begin{pmatrix} 1 & X_1 \\ \vdots & \vdots \\ 1 & X_n \end{pmatrix}, \beta = \begin{pmatrix} \beta_0 \\ \beta_1 \end{pmatrix}, \mathbf{W} = \begin{pmatrix} w_1 & & 0 \\ & \ddots & \\ 0 & & w_n \end{pmatrix}$$

where $y_i = \sigma_{reli}$ or α_{reli}, w_i = corresponding error $E[\sigma_{reli}]$ or $E[\alpha_{reli}]$ raised to the -2, and X_i = a star parameter of the i^{th} star. This will give us the corresponding simplified matrix equation analog of Equation 3.15:

$$WSS\left(\beta\right) = (\mathbf{y} - \mathbf{X}\beta)^T\mathbf{W}(\mathbf{y} - \mathbf{X}\beta) \tag{3.16}$$

The process for minimization can be simplified by defining a new set of matrices:

$$\tilde{\mathbf{y}} = \sqrt{\mathbf{W}}\mathbf{y}$$

$$\tilde{\mathbf{X}} = \sqrt{\mathbf{W}}\mathbf{X}$$

to once again rewrite Equation 3.16:

$$WSS\,(\beta) = (\tilde{\mathbf{y}} - \tilde{\mathbf{X}}\beta)^T(\tilde{\mathbf{y}} - \tilde{\mathbf{X}}\beta) \tag{3.17}$$

Now that we have a convenient form, the minimization is straightforward as setting the derivative of WSS with respect to β equal to 0:

$$\begin{aligned}\frac{\partial WSS}{\partial \beta} &= \frac{\partial}{\partial \beta}(\tilde{\mathbf{y}} - \tilde{\mathbf{X}}\beta)^T(\tilde{\mathbf{y}} - \tilde{\mathbf{X}}\beta) \\ &= \frac{\partial}{\partial \beta}\left(\tilde{\mathbf{y}}^T\tilde{\mathbf{y}} - 2\beta^T\tilde{\mathbf{X}}^T\tilde{\mathbf{y}} + \beta^T\tilde{\mathbf{X}}^T\tilde{\mathbf{X}}\beta\right) \\ &= 0 - 2\tilde{\mathbf{X}}^T\tilde{\mathbf{y}} + 2\tilde{\mathbf{X}}^T\tilde{\mathbf{X}}\beta \overset{\text{set}}{=} 0\end{aligned}$$

which yields a solution for the best-fit line parameters:

$$\beta = \left(\tilde{\mathbf{X}}^t\tilde{\mathbf{X}}\right)^{-1}\tilde{\mathbf{X}}^T\tilde{\mathbf{y}} \tag{3.18}$$

Using the relative variability, relative maximum, their associated errors, and the solutions for the weighted best-fit line parameters, we generate a series of plots of relative variability and relative maximum vs. various star parameters: B-V magnitude (ratio of flux in blue vs. orange parts of electromagnetic spectrum, which is a tracer of the surface, or photospheric, temperature of a star), effective temperature, rotational period, and $\log(R'_{HK})$ (chromospheric contribution to the stellar spectrum near the Ca II H and K lines). Utilizing the polyfit python package, the solutions for the weighted and unweighted best-fit parameters for Figure 3.4 are visible within the figure caption.

Upon careful examination of the trends within the best-fit lines, it is apparent that the linear models produced by the weighted fits do not entirely align with the actual measurements. This can be attributed to the $\frac{1}{\text{Error}^2}$ nature of the weights, which results in the lines being pulled down towards the flat levels at the bottom of the plots. This is due to the fact that the lower the relative variability, the higher the precision, and thus the weights are increased. Consequently, points with higher precision are assigned greater weight, resulting in their strong influence within the weighted linear fits. Therefore, it is crucial to consider the unweighted linear fits in our analysis, as the importance of points within the weighted linear fits can become inflated due to the way in which the uncertainties on the relative variability are defined.

Furthermore, close binary star systems were included in the plots but excluded from the linear fits in the context of this thesis. Close binary systems display enhanced UV activity owing to the interaction of their magnetospheres, which are not representative of single-star systems that are the primary focus of this thesis.

Analysis of the unweighted relative variability subplots in Figures 3.4A, C, E, and G, we observe significant correlations between relative variability and various stellar parameters. Specifically, Figure 3.4A indicates a positive relationship ($\sim 2.5\sigma$) between relative variability and B-V color, while Figure 3.4C shows a negative relationship ($\sim 3\sigma$) between relative variability and effective temperature (confirming the trend observed in Figure 3.4A). In addition, Figure 3.4E reveals a positive relationship ($\sim 2.2\sigma$) between relative variability and rotational period, and Figure 3.4G demonstrates a positive relationship ($\sim 1.4\sigma$) between relative variability and $\log(R'_{HK})$. Therefore, increases in B-V magnitude, rotational period, and $\log(R'_{HK})$ generally lead to increases in relative variability.

When looking at the relative maximum subplots shown in Figures 3.4B, D, F, H, there are certain outlier stars that demonstrate notably large relative maximums, reaching as high as $\sim 3.5 - 5.5\mu$. These outliers correspond to stars with strong stellar flare activity, particularly low-mass single star systems (M type dwarfs) and binary systems. The interaction between companion stars in binary systems, such as the RS CVn systems mentioned in Section 2, can lead to enhanced magnetic activity and flare magnitudes, resulting in greater relative maximums (Osten & Brown, 1999).

3.2 FUV Periodicity: Lomb-Scargle Analysis

In our analysis of the FUV periodicity for stars within our sample, we utilized two mathematical techniques for frequency deconstruction and signal denoising: Fourier transforms and wavelet transforms. These mathematical tools are widely used in many scientific fields and are particularly useful in analyzing complex data sets such as time-series data.

Fourier transforms work on the principle that any periodic function can be broken down into an infinite sum of sine and cosine waves. The Fourier transform is a mathematical technique used to decompose a signal into its frequency components. This is done by taking a function, $x(t)$, and performing a transformation from time domain to frequency domain using the equation:

$$X(\omega) = \int_{-\infty}^{\infty} x(t) e^{-i\omega t} dt \tag{3.19}$$

where $X(\omega)$ is the power of coefficient and ω is the continuous frequency. However, since we are dealing with a discrete data set, we cannot use continuous function mathematics. Therefore, the discrete analog of the Fourier transform is used, where we transform a discrete data set, $x(n)$, from n-space to frequency space using the equation:

$$X(k) = \sum_{n=0}^{N-1} x(n) e^{-i\omega_k n} \tag{3.20}$$

where $k = 0, 1, \cdots, N-1$ and ω_k is the discrete frequency.

Wavelet transforms, on the other hand, decompose a signal into wavelets, which are localized in both frequency and time domains. Wavelets come in many shapes and sizes, with specific wavelets optimized for specific tasks. The wavelet transform is a mathematical technique used to analyze a signal in both time and frequency domains. It is given by:

$$X_\omega(\tau, s) = \frac{1}{\sqrt{|s|}} \int_{-\infty}^{\infty} x(t) \overline{\psi} \left(\frac{t-\tau}{s} \right) dt \tag{3.21}$$

where s is the scale factor of the wavelet, τ is the temporal translation of the wavelet, and $\overline{\psi}$ is the chosen wavelet. Since we are using a discrete data set, we utilize the discrete wavelet transform. The discrete wavelet transform is given by:

$$\Psi_x[n, a^j] = \frac{1}{\sqrt{a^j}} \sum_{m=0}^{N-1} x[m]\psi\left(\frac{m-n}{a^j}\right) \tag{3.22}$$

where a^j is the scaling factor, ψ is the wavelet function, m represents the timesteps of the wavelet, and n represents the translation of the wavelet.

Fourier and wavelet transforms are two commonly used mathematical techniques in signal analysis. One of the key differences between the two is that Fourier transforms provide excellent frequency resolution but lack time resolution, while wavelet transforms provide a balance of both time and frequency resolution. This is due to the fact that wavelets are localized functions that can capture temporal frequencies, allowing for the analysis of non-stationary signals.

Fourier's decomposition of a signal into a sum of sine and cosine waves is an excellent method for analyzing stationary signals that do not change over time. However, it is not as effective when analyzing signals that change over time, as it fails to provide information on how the frequency components of the signal evolve over time. In contrast, wavelet transforms use wavelet functions that are more localized in time and frequency, making them better suited for analyzing non-stationary signals.

Wavelet transforms can capture both high and low frequency components of a signal, as well as their temporal evolution. This is achieved by stretching or compressing the wavelet function in time and frequency domains, thus adjusting the scale of analysis. By using wavelet transforms, we can detect changes in the signal that may occur over a specific time period, which is useful for analyzing complex signals that exhibit non-stationary behavior. Additionally, wavelet transforms can also be used to analyze signals with irregular time intervals, such as those with missing or unevenly spaced data points.

In addition to their usefulness in analyzing non-stationary signals, wavelet transforms also offer a powerful tool known as soft thresholding. When performing wavelet transform decomposition, the resulting coefficients may be dominated by signal noise, obscuring the underlying signal. Soft thresholding is a technique used to denoise signals by removing or shrinking the coefficients that correspond to noise, leaving only the coefficients that represent the signal. This is achieved by applying a threshold to the coefficients, with values below the threshold being set to zero, while those that are above being shrunk. Soft thresholding can be particularly effective when dealing with signals that have a mixture of smooth and sharp features, as it can preserve the sharp features while removing the noise in the smooth regions.

As we are searching for periodicities visible within our sample of stars, the Fourier transform becomes the natural choice for statistical analysis of the frequencies hidden within each stars' emission pattern. This allows for an extraction of any relevant frequency information that may be encoded within each particular light curve. However, due to the nature of measurement, there is inevitably noise within a sample, which will permeate through the Fourier transform. As a result, we can denoise the output of the Fourier transform utilizing the soft thresholding technique available with wavelet transforms.

To perform discrete Fourier transform computations on our data sets, we utilized the Lomb-Scargle Periodogram package[2] . Additionally, we utilized the PyWavelets package[3] for wavelet denoising. From this, we are able to transform the flux as a function of time, Table 2.3, into a frequency and their associated power graph, Figure 3.2. Visible within Figure 3.2 is the deconstruction of each individual ion into its frequency domain (Given by the left-most column), as well as increasingly greater levels of soft thresholding. Each successive column's threshold is calculated via the keep coefficient, which dictates the percentage of wavelet coefficients to be kept after the soft thresholding (e.g. 1 indicates no denoising, 0.5

[2] `https://docs.astropy.org/en/stable/timeseries/lombscargle.html`
[3] `https://pywavelets.readthedocs.io/en/latest/`

indicates 50% of wavelet coefficients are kept).

The method with the most visually appealing results, which minimizes signal loss while maximizing noise reduction, is selected for further refinement. This process includes utilizing two discrete data set mathematical techniques: Linear interpolation and root-mean-squares (RMS). These mathematical tools are widely used on incomplete data sets, or for combining data sets.

Interpolation is a technique used to estimate the value of a function or data point between two known values. Although there are many ways of doing this, depending on the goals and input data set, the linear interpolation method assumes that the data changes linearly between these known points. The estimation is mathematically described as:

$$y(x) = \frac{y_2 - y_1}{x_2 - x_1} x(x - x_1) + y_1 \tag{3.23}$$

where x is the value of the desired interpolated point, y is the value at x, (x_i, y_i) are the 2 known points surrounding x. Given this interpolation scheme, it becomes possible to map a signal onto any arbitrary frequency map, provided that (x_i, y_i) exist.

RMS, although a simple mathematical measurement performed by:

$$RMS = \sqrt{\sum_{i=1}^{n} x_i^2} \tag{3.24}$$

where x_i is a data point, is an incredibly powerful tool in regards to signal processing. The RMS value is particularly useful for measuring the strength or amplitude of a signal.

Using linear interpolation, and RMS, it becomes possible to interpolate the ion frequency decompositions of a specified column of Figure 3.2 to a common frequency map. From here, we can RMS the data points together to get a comprehensive description of the UV emission periodicity of a particular star. In regards to computation, we use the built-in interpolation functions of the scipy package[4] , to produce the RMS graph illustrated in

[4] `https://scipy.org/`

Figure 3.3.

Each peak that has a power (P) subtracted by the mean $> 2.58\sigma$ (Corresponding to a significance level of 99%) is recorded in Tables 3.1, 3.2, 3.3, 3.4, and 3.5, according to their respective stars. It should be noted that calculations regarding the presence of significant peaks can be distorted by sample size and distribution of measurements. This can lead to artificial period measurements for extremely low and extremely high periods, and as a result, it should be disregarded if peak period is larger than the total length of observation for a specific star. Keeping this in mind, the most significant periods for each star is: HST α Centauri A: 133.5 days (Significance $\approx$ 2.8), HST α Centauri B: 209.2 days (Significance $\approx$ 3), IUE α Centauri B: 210.1 days (Significance $\approx$ 3.7), IUE ϵ Eri: 156.3 days (Significance $\approx$ 3.5), and IUE ξ Boo: 79.0 days (Significance $\approx$ 6). The concurrence between the measurements obtained from both HST and IUE for α Centauri B, exhibiting a high level of statistical significance, strongly suggests the existence of a cycle in the stellar UV activity of α Centauri B with a period of approximately 210 days.

Table 3.1. Periodicity Analysis of HST α Centauri A

Ions	Peak Period days	Peak Significance $\frac{P-\mu}{\sigma}$
Si III	9304.81	3.34
	5582.88	3.45
	3987.77	3.12
	3101.60	2.63
N V	9304.81	3.52
	5582.88	3.70
	3987.77	3.44
	3101.60	3.03
	133.56	2.67
C II	9304.81	3.22
	5582.88	3.38
	3987.77	3.21
	3101.60	2.90
	133.56	2.59
Si IV	9304.81	3.29
	5582.88	3.45
	3987.77	3.27
	3101.60	2.93
	133.56	2.86
	132.30	2.68
	92.74	2.64
RMS	9337.92	3.61
	5606.74	3.77
	3894.84	3.48
	3116.34	3.10
	133.51	2.81

Note. — Peaks in corresponding ion emission bands for HST α Centauri A, and RMS (root-mean-square). Period in (*days*), and significance is standard normal variable of period power.

Table 3.2. Periodicity Analysis of HST α Centauri B

Ions	Peak Period days	Peak Significance $\frac{P-\mu}{\sigma}$
Si III	215.20	2.94
	209.14	2.86
C II	215.20	2.59
	209.14	2.59
Si IV	209.14	2.60
RMS	209.21	2.30
	76.12	2.61

Note. — Peaks in corresponding ion emission bands for HST α Centauri B, and RMS (root-mean-square). Period in (*days*), and significance is standard normal variable of period power.

Table 3.3. Periodicity Analysis of IUE α Centauri B

Ions	Peak Period days	Peak Significance $\frac{P-\mu}{\sigma}$
C II	3643.59	2.30
	3260.05	2.82
	1015.43	3.35
	983.19	3.17
	952.94	2.61
	848.51	3.35
	825.88	3.27
	578.89	2.62
	568.27	2.93
	472.83	2.70
	465.72	3.349
	327.73	2.62
	205.78	2.97
	204.43	3.12
	203.09	2.77
	199.17	2.67
	197.89	3.11
	40.56	2.81
	40.51	3.51
	39.58	3.11
	39.53	3.52
	39.45	3.34
	38.12	3.22
	37.84	3.14
	37.79	3.71
	37.75	3.14
Si IV	812.45	2.84
	625.68	2.84
	611.62	2.65
	227.76	2.97
	220.38	2.95
	210.17	3.51
	208.56	2.67

Table 3.3 (cont'd)

Ions	Peak Period days	Peak Significance $\frac{P-\mu}{\sigma}$
	129.91	2.97
	129.30	3.13
RMS	812.66	3.23
	625.73	2.98
	227.79	3.08
	220.37	3.07
	210.13	3.69
	129.31	3.30

Note. — Peaks in corresponding ion emission bands for IUE α Centauri B, and RMS (root-mean-square). Period in (*days*), and significance is standard normal variable of period power.

Table 3.4. Periodicity Analysis of IUE ϵ Eri

Ions	Peak Period days	Peak Significance $\frac{P-\mu}{\sigma}$
C II	1894.84	2.77
	1754.48	3.04
	1633.48	3.16
	1528.10	3.02
	158.43	2.72
	157.38	3.35
	156.34	3.78
	155.31	3.57
	154.30	3.03
	123.68	3.07
	123.04	3.02
	96.87	3.11
	96.48	3.58
	96.09	3.66
	95.70	3.46
	39.77	2.88
	39.71	3.43
	39.64	3.61
	39.57	3.04
	35.27	2.65
Si IV	297.93	2.94
	294.23	3.32
	238.05	2.69
	212.43	3.03
	210.54	3.44
	181.50	3.03
	180.12	3.46
	178.76	3.39
	177.42	2.86
	154.30	2.87
	153.30	3.23
	152.32	3.33
	151.35	3.21

Table 3.4 (cont'd)

Ions	Peak Period days	Peak Significance $\frac{P-\mu}{\sigma}$
	127.00	3.58
	55.15	3.40
	55.02	4.15
	54.89	3.53
	51.32	2.71
	51.21	2.76
	48.99	2.68
	237.98	2.63
RMS	156.33	3.47
	55.02	3.06
	39.64	2.81

Note. — Peaks in corresponding ion emission bands for IUE ϵ Eri, and RMS (root-mean-square). Period in (*days*), and significance is standard normal variable of period power.

[t]

Table 3.5. Periodicity Analysis of IUE ξ Boo

Ions	Peak Period days	Peak Significance $\frac{P-\mu}{\sigma}$
	512.94	2.69
	461.22	3.07
	152.88	4.52
	152.04	5.41
	151.12	5.43
	150.37	5.12
	149.55	4.17
	83.29	2.64
C II	83.03	3.19
	82.78	3.19
	76.34	3.33
	76.12	3.12
	40.75	2.66
	40.69	3.83
	40.63	4.81
	40.57	5.02
	40.51	4.82
	40.45	3.09
	211.92	4.25
	210.29	3.82
	147.94	2.61
	123.89	2.60
	89.24	2.75
	84.05	2.71
	83.79	6.04
	83.54	5.19
	83.29	3.08
	78.97	6.31
	78.74	5.30
Si IV	78.52	2.95
	68.18	2.82
	68.01	4.10
	67.84	2.77

Table 3.5 (cont'd)

Ions	Peak Period days	Peak Significance $\frac{P-\mu}{\sigma}$
	57.71	2.75
	57.59	3.00
	57.47	2.71
	53.65	2.75
	53.55	2.63
	44.73	3.78
	43.32	3.80
	43.25	3.07
	211.83	3.93
	152.04	3.28
	83.79	5.66
RMS	78.96	6.04
	68.09	3.92
	57.59	2.64
	44.73	3.41
	43.32	3.53

Note. — Peaks in corresponding ion emission bands for IUE ξ Boo, and RMS (root-mean-square). Period in (*days*), and significance is standard normal variable of period power.

Chapter 4

Results: Modest long term FUV variability on most cool stars

Figure 3.4C shows that an increase in the effective temperature of a star, which is an indication of its mass, is associated with decreased relative variability in the chromosphere of the star as traced by the observed UV lines. Our sample of stars in this study primarily comprises of cool stars with spectral types ranging from M to F, corresponding to effective temperatures of roughly 3000 – 7000 K and stellar masses of approximately 0.1 – 2.0 solar masses. Each star emits a total flux output known as the Bolometric flux, which is calculated by integrating the flux measurements over all frequencies.

$$F_{Bol} = \int_0^\infty F_\nu d\nu \tag{4.1}$$

where ν is a particular frequency, and F_ν is the flux measurement corresponding to said frequency. As stars age, most spectral types exhibit a significant decline in the magnitude of fractional power of UV flux compared to Bolometric flux. This decline in fractional UV flux begins rapidly in most stars, but it remains constant for M type stars up to ages of 240 ± 30 Myr (Loyd et al., 2021). This suggests a slower fractional UV evolution for low-mass stars. Consequently, many M type stars have higher fractional UV flux than their more massive counterparts, resulting in higher UV energy per unit power than F, G, and K stars. UV flux is strongly linked to the magnetic activity within a star, as UV energy is emitted from the chromosphere and corona of a star. Therefore, greater fractional UV flux is associated with more magnetically active upper stellar atmospheres (Wood et al., 1997), leading to higher relative variability. This higher relative variability would then be reflected in greater experimentally measured relative variability for these low-mass M type stars. Given that lower mass stars have lower effective temperatures, this experimentally derived negative correlation between effective temperature and relative variability confirms our findings.

In Figure 3.4E, a weak (with a significance of approximately 2σ) positive correlation between the rotational period (P_{rot}) and relative variability (σ_{rel}) is demonstrated, which contradicts the expected relationship between rotation and UV activity. Previous studies have shown that cool stars have more intrinsic variability (likely driven by unresolved stellar flares) and that the rotational period and UV activity have a power law decline with a slope coefficient of approximately -1.1 (France et al., 2018) (Indicating $P_{rot} \propto UV^{-1.1}$). These studies indicate that stars with longer rotational periods (rotating slower) have lower levels of UV activity compared to those with shorter rotational periods (rotating faster). Further investigation of the data revealed that the positive correlation in our model is driven by an outlier star with high relative variability at a period greater than 80 days (Proxima Centauri). We also found a weaker positive correlation (with a significance of approximately 1.4σ) between the relative variability and the strength of the chromospheric Ca II emission lines in Figure 3.4G, which agrees with accepted correlations but is not statistically significant. The lack of a strong correlation between stellar activity indicators (P_{rot} and $\log R'HK$) and relative variability may be due to the small number of objects with multi-epoch observing campaigns, as there are few objects with low activity ($Prot > 30$ days or $\log R'_{HK} < 5.0$) in the sample used in this study.

Despite the aforementioned limitations, the analysis presented here indicates a lack of significant far-ultraviolet (FUV) variability among cool stars on a large scale. The large amplitude peaks in relative maximum values are only observed in very active stars and close binaries, and there is no corresponding minimum observed. The FUV fluxes observed in a quiescent spectrum should be representative of the average quiescent flux of the star at timescales of years.

Chapter 5

Summary

Exoplanetary atmospheres are affected by UV radiation inputs from their host stars at largely varying timescales, which can influence the photochemical equilibrium of exoplanetary atmospheric conditions and their susceptibility to atmospheric escape. While studies of X-ray/UV flare properties and long-term stellar evolution of exoplanet host stars have shed light on constraints regarding stellar inputs to exoplanetary systems, the UV temporal variability of cool stars on the timescale of stellar cycles has remained unexplored in the astronomical science society. However, in this honors thesis, we present a comprehensive investigation of the temporal UV variability of cool stars. The FUV emission lines, analyzed within this thesis, that trace the chromosphere and transition region activity were analyzed using data from *HST* and *IUE* data archives to evaluate the characteristic variability of cool stars on the desired timescales. It was found that the relative variability of FUV light curves decreases with increasing stellar temperature, and a weak positive trend in the temporal variability with the Ca II R'_{HK} stellar activity indicator was observed. Additionally, various periodic structures within FUV flux of select data sets were detected, requiring further examination to identify potential false-periodic sources.

Bibliography

Ahrer, E.-M., Alderson, L., Batalha, N. M., et al. 2023, Nature, 614, 649, doi: 10.1038/s41586-022-05269-w

Ayres, T. R. 1991, , 375, 704, doi: 10.1086/170236

Boro Saikia, S., Marvin, C. J., Jeffers, S. V., et al. 2018, A&A, 616, A108, doi: 10.1051/0004-6361/201629518

Charbonneau, D., Brown, T. M., Latham, D. W., & Mayor, M. 1999, The Astrophysical Journal, 529, L45, doi: 10.1086/312457

Dere, K. P., Landi, E., Young, P. R., et al. 2009, , 498, 915, doi: 10.1051/0004-6361/200911712

Dressing, C. D., & Charbonneau, D. 2015, The Astrophysical Journal, 807, 45, doi: 10.1088/0004-637X/807/1/45

France, K., Arulanantham, N., Fossati, L., et al. 2018, , 239, 16, doi: 10.3847/1538-4365/aae1a3

France, K., Loyd, R. O. P., Youngblood, A., et al. 2016, The Astrophysical Journal, 820, 89, doi: 10.3847/0004-637X/820/2/89

Harman, C. E., Schwieterman, E. W., Schottelkotte, J. C., & Kasting, J. F. 2015, The Astrophysical Journal, 812, 137, doi: 10.1088/0004-637X/812/2/137

Jakosky, B., Brain, D., Chaffin, M., et al. 2018, Icarus, 315, 146, doi: https://doi.org/10.1016/j.icarus.2018.05.030

Lammer, H., Selsis, F., Ribas, I., et al. 2003, The Astrophysical Journal, 598, L121, doi: 10.1086/380815

Loyd, R. O. P., Shkolnik, E. L., Schneider, A. C., et al. 2021, The Astrophysical Journal, 907, 91, doi: 10.3847/1538-4357/abd0f0

Loyd, R. O. P., Schneider, P. C., Jackman, J. A. G., et al. 2023, , 165, 146, doi: 10.3847/1538-3881/acbbc8

MacGregor, M. A., Weinberger, A. J., Loyd, R. O. P., et al. 2021, , 911, L25, doi: 10.3847/2041-8213/abf14c

Mayor, M., & Queloz, D. 1995, Nature, 378, 355, doi: 10.1038/378355a0

Osten, R. A., & Brown, A. 1999, The Astrophysical Journal, 515, 746, doi: 10.1086/307034

Teal, D. J., Kempton, E. M. R., Bastelberger, S., Youngblood, A., & Arney, G. 2022, , 927, 90, doi: 10.3847/1538-4357/ac4d99

Tian, F., Kasting, J. F., Liu, H.-L., & Roble, R. G. 2008, Journal of Geophysical Research: Planets, 113, doi: https://doi.org/10.1029/2007JE002946

Tsai, S.-M., Lee, E. K. H., Powell, D., et al. 2022, Direct Evidence of Photochemistry in an Exoplanet Atmosphere. https://arxiv.org/abs/2211.10490

Wood, B. E., Linsky, J. L., & Ayres, T. R. 1997, , 478, 745, doi: 10.1086/303821